Powder Technology 371 (2020) 96–105

Contents lists available at ScienceDirect

Powder Technology

journal homepage: www.elsevier.com/locate/powtec

Cohesivity assessment of semi-crystalline and crystalline powders using a Warren Springs cohesion tester

Camila G. Jange [a], Pumu Taku [b], Shuyi Peng [a], Michelle P. Dixon [a], Abhishek Shetty [c], R.P. Kingsly Ambrose [a,*]

[a] Department of Agricultural and Biological Engineering, Purdue University, West Lafayette, IN, USA
[b] National Dairy Research Institute- ICAR, Karnal, India
[c] Rheology Division, Anton Paar USA, Ashland, Virginia, USA

ARTICLE INFO

Article history:
Received 3 December 2019
Received in revised form 4 March 2020
Accepted 21 May 2020
Available online 23 May 2020

Keywords:
Cohesion
Solid state matrix
High strain
Particle morphology

ABSTRACT

The direct measurement of cohesion under high strain and the quantitative effects of solid matrix structure on particle morphology and bulk rheology have not been explored thoroughly in literature. A Warren Springs geometry installed on an air bearing rotational rheometer capable of capturing the amount of shear stress required for powder failure at a wide range of initial consolidation states was implemented in the study to measure the cohesion trend of over-consolidated powder materials. Wheat, potato, corn starches and microcrystalline cellulose (MCC PH101) powders were analyzed. MCC PH101 powder exhibited the highest weighted cohesion strength among the powders at all consolidation stresses because of the high particle aspect ratio given the inherited crystallinity of its compositional matrix. MCC sample also had greater variation between incipient and steady state portions of the torque profile attributable to its characteristic particle stiffness, which, consequently, yielded in distinct particle deformation behavior.

1. Introduction

The flow property of particulate materials is a critically important parameter in many handling and processing operations and greatly influences the relative efficiency of transportation, separation, mixing, compression, and packaging. For compositionally diverse powders, irrespective of uniformity in size, the complexity in shape distribution and composition dictates their flow behavior [1,2]. This is because, in general, differences in the morphological attributes in powder materials influence the mechanical and the interparticle interaction characteristics of the product.

The quantitative assessment of flow is mostly intended to estimate the dynamic, shear flow patterns and compressibility of powders. Powder with high plastic deformation characteristics will have a higher compressibility. The increase in percent compressibility of a powder depends on their viscoelastic properties, besides intermolecular and morphological effects that include changes in surface roughness, particle size, shape factors, and composition of particles within the bulk [3–5].

In a shear cell test, a powder loaded at a normal stress undergoes inelastic deformation. For hopper and silo designs, these devices typically operate under high stress and low strain flow mode with initial solid fraction in the under-consolidated state. The change in stress will affect the bulk density depending on the consolidation and dilatational behavior of the powder. Powders with poor flow behavior are expected to consolidate, which results in increasing the bulk density. The magnitude of the load required for the powder to yield is the indicator of flowability [6]. For cohesive powders, shear cell instruments, designed to characterize the flow behavior of particulates, are limited to work at higher normal stress loads, where the shear stresses are approximated to a linear correlation with the normal stress using the Mohr-Coulomb model. Nonetheless, at low stresses, the yield loci curve follows an exponential profile, widely, known as the Warren-Spring model. Therefore, in most cases, determination of the cohesion index $(0, \tau)$ from a shear cell analysis requires extrapolation of the yield loci. This is a problem when designing processes as such extrapolation may result in over prediction of stress distributions and, hence, conservative critical outlet width in hopper and silo designs [7]. Peleg et al. [8] demonstrated the possibility to obtain a more accurate prediction of the principal stresses, cohesion, and tensile strength of cohesive powders from the Warren-Spring model using the Mathematica Player® open source software.

The Warren Springs (WS) testing like other Warren Springs testers, including the Warren Spring Bradford Cohesion Tester (WSBCT) [9], offers versatility for the direct assessment of the cohesion strength. The measurement, however, comprises the compaction of a powder bed using a vented piston and the penetration of the WS geometry that produces an over-consolidated powder bed. The powder bed confined into the vanes of the WS geometry is subjected to a torque, which, then, computes the resistance of the powder sliding as a cohesion strength

* Corresponding author at: Department of Agricultural and Biological Engineering, 225 S University Street, West Lafayette, IN 47907, USA.
E-mail address: rambrose@purdue.edu (R.P.K. Ambrose).

https://doi.org/10.1016/j.powtec.2020.05.077
0032-5910/

profile [10]. Mathematically, the cohesion strength can be derived from a moment balance by correlating the shear resistance to the applied torque (T) as in Eq. (1):

$$dT = S(\pi r^2 dr) \tag{1}$$

where, S is the shear strength of the powder at failure and r is the radius of the vane.

To obtain the total torque (T) across the area, the integration from $r = R_i$ (inner radius of vanes) to $r = R_0$ (outer radius of vanes) is conducted as in Eq. (2):

$$\int_0^T dT = \int_{Ri}^{R0} 2\pi r^2 dr \tag{2}$$

Rearranging (2):

$$S = \frac{3T}{2\pi\left(R_o^3 - R_i^3\right)} = \left[\frac{N}{m^2}\right] \tag{3}$$

It is noteworthy that the cohesion strength is measured at the maximum penetration force required during the penetration step. The penetration force depends, evidently, on the pre-compaction load applied using the vented piston. This method is unable to calculate the principal stresses acting in the powder bed directly because it does not ensure the pre-shear step adapted in conventional shear cell devices [6]. Another limitation of the Warren-Springs test is that it relies on the characterization of flow patterns under high strain conditions because the penetration step of the WS geometry causes over-consolidation of the powder bed, which invalidates its application in hopper/silo design [9]. However, the WS test can be of primary interest for dense flow operations under high-strain condition, such as in high shear granulation and high shear mixing. The understanding of the cohesive nature of different powder intermediates and/or products under high-strain can help in the optimization of the shear input from lab to commercial scale operations.

Powder flow assessment at high strain and high stress conditions is a complex phenomenon that requires a fundamental approach. Understanding powder cohesivity, which can be used for effective design of processing equipment under high strain conditions, as a function of particle morphology and compressibility characteristics remains an underexplored area. Therefore, the primary objective of this work was to evaluate the effect of particle characteristics and the morphological effects of solid-state matrix on powder cohesivity. This work also provides a preliminary evaluation of the compaction trend of primary particles and agglomerates on the kinematic profile as well as a description of the time dependence of plastic transition for different powder samples.

2. Materials and methods

2.1. Sample preparation

Samples of native (unmodified) starch sources- corn (Sigma Aldrich, Saint Louis, MO), wheat (Sigma Aldrich, Saint Louis, MO), potato (Sigma Aldrich, Saint Louis, MO), and microcrystalline cellulose (MCC, grade PH101, FMC Corporation, Newark, DE) were used in this study. To enable proper comparison, the starch samples were dried at 60 °C for 5 h in an oven to a moisture content closer to that of MCC. A halogen moisture content analyzer (Mettler Toledo HG63, Greifensee, Switzerland) was used to measure the moisture content of the samples before and after drying. An aluminum sample pan was weighed with, approximately, 3.00 g of sample and leveled to 105 °C until moisture content stabilization (10 min). The samples were then stored at 5 °C until the measurements to avoid moisture uptake and the influence of environmental conditions. Water activity of the samples, to confirm the drying efficiency, were performed using a Decagon AcquaLab 3TE (Decagon Devices, Pullman, WA).

2.2. Measurement of particle size and shape

Particle size and shape were measured using the Morphologi G3-ID (Malvern Instruments, Worcestershire, UK) following the ISO 13322-2 standard [11]. The samples were dispersed on a glass plate (180 × 110 mm) by means of pressurized air at 1 kPa and the objective lens was set at × 5 (65 μm – 420 μm). Aspect ratio values close to unity indicated circular shape characteristics. The average number of particles analyzed was 100,000 per replicate (× 3). Two-dimensional images of the samples were obtained to compare with the shape characterization using the Morphology G3-ID optical system (Nikon CFI 60) set at × 5.

2.3. Bulk density and compressibility characterization

The bulk density of the samples was measured using a 100 mL graduated cylinder filled gravimetrically up to 50 mL. The bulk density was calculated from the mass -volume ratio of powder loaded in the graduated cylinder.

The compaction trend of the samples was evaluated by direct compression of the powder bed at a consolidation stress range of 0 to 15 kPa. The compressibility index was calculated based on the Carr's index, C, expressed in terms of compressibility percent (Eq. (4)):

$$C = \left(1 - \frac{\rho_B}{\rho_C}\right).100 \tag{4}$$

where, ρ_B is the aerated bulk density and ρ_C is the conditioned bulk density.

2.4. Warren Springs cohesion strength test

An Anton Paar MCR-502 rheometer equipped with the Warren Springs geometry was used for the measurements. The refrigerated samples were equilibrated to ambient conditions (average temperature and relative humidity, respectively, were 25 °C and 40%) in sealed bags for 1 h prior to the start of the measurement and, then, transferred to the measuring cylinder (radius of 50 mm and total volume of 140 mL) gravimetrically up to the mark of 45 mL. Samples were pre-compacted for 60 s with an air permeable piston (radius of 48 mm) to remove interstitial air and to adjust the powder bed height using defined normal loads of 0.25, 0.5, 1, and 3 kPa. Subsequently, a penetration step was performed using the Warren Springs geometry on the MCR rheometer. The overall outer and inner diameter of the tester were 36 mm and 6 mm, respectively. The tester contained 8 vanes of 3 mm thickness and 10 mm height. Further reference on the rheometer features is provided in Mishra et al. [12]. During the penetration step no rotation was applied to the shaft and a plot of normal stress versus displacement was obtained (Fig. 1a). In this study, the penetration step was conducted for 80 s with collection of 160 data points per second. The maximum displacement was set as 10 mm down the powder bed that was accompanied by a sample over-consolidation step where the normal stress was raised, for example, from 0.23 N to 1.7 N as in Fig. 1a. The normalized penetration depth was calculated based on the ratio of the actual blade height divided by the maximum displacement achieved (which was 9.938 mm for starch samples). The area under the normal force versus displacement in the penetration step was used to obtain the work required during downward travel of the Warren Springs geometry. After the penetration step, the cohesion strength measurement (Fig. 1b) was performed using the Warren Springs geometry (Fig. 1c), where the applied normal force was regarded as radially distributed [10]. The step of cohesion strength measurement was set to 40 s with collection of 8000 points per second. The weighted cohesion was

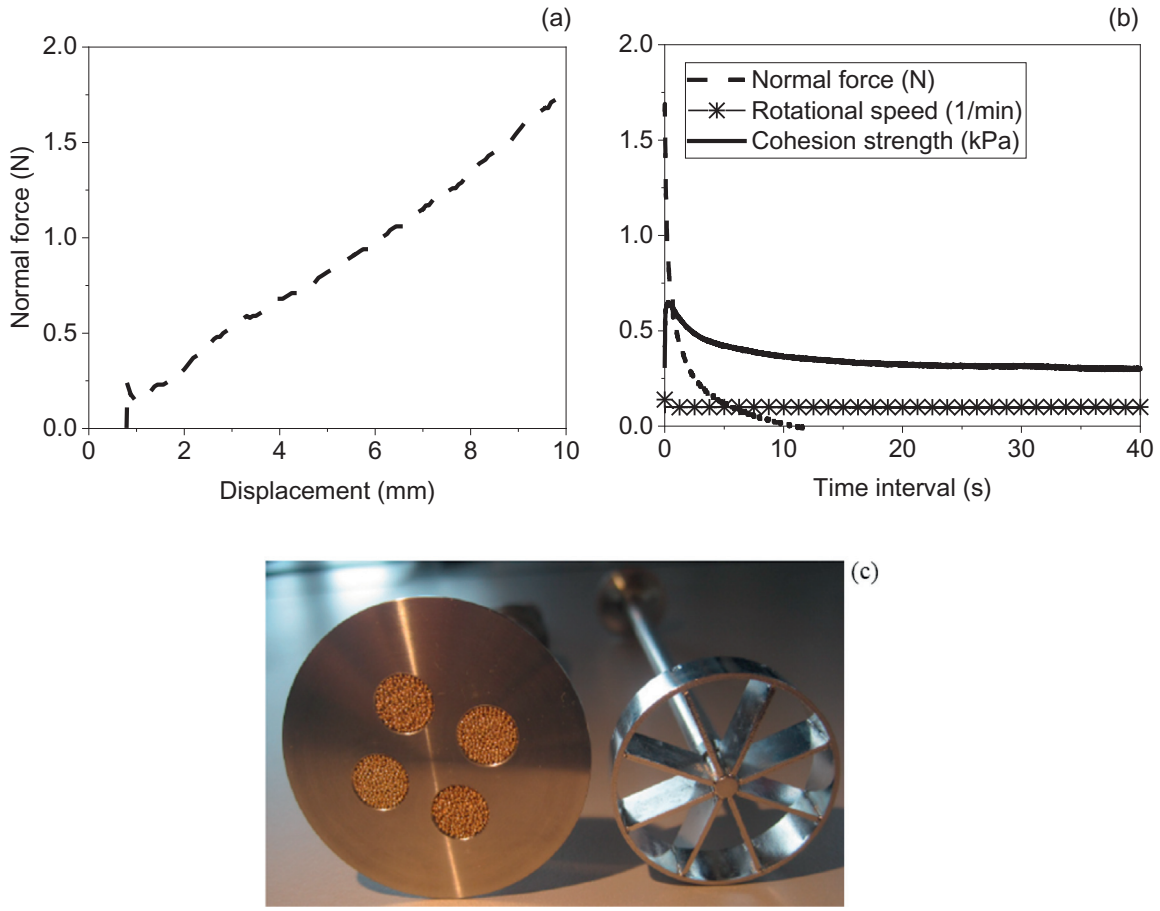

Fig. 1. Cohesion strength profile: (a) Penetration step, (b) Cohesion strength measurement, (c) vented piston on the left and Warren Springs cohesion test on the right side.

calculated by dividing the cohesion strength values by the aerated bulk density.

2.5. Prediction of cohesion strength

A statistical model was developed to predict the cohesion strength based on the particle properties. A data set was constructed excluding the MCC PH101 data points. A best subset selection procedure was implemented to select the best predictive model based on specified criterion, including adjusted coefficient of multiple determination (R^2_{adj}), mean square error (MSE), Mallow's C_p, prediction sum of squares (PRESS), and variable inflation factor (VIF). To account for the adequacy of the multiple linear regression assumptions, diagnostic plots before and after transformation of the predicted and independent variables were examined. The variable inflation factor was calculated to ensure that multicollinearity issues were not present. As a rule of thumb, VIF of 10 indicates excessive multicollinearity of a certain parameter.

2.6. Statistical analysis

Analysis of variance (ANOVA) followed by Tukey's mean comparison test evaluated the statistical significance between the samples' kinematic profiles at 95% significance level using SAS 9.3 software (SAS Institute Corporation, Cary, NC, U.S.A.). The weighted least squares correction was applied prior to the ANOVA test to fix the heteroscedasticity of the residuals. All the measurements were conducted in triplicate.

3. Results and discussion

3.1. Particle morphology

The moisture content of the samples before and after drying as well as the water activity, volume mean diameter, and mean aspect ratio are given in Table 1. The moisture content of the samples prior to testing did not differ significantly ($p > .05$). The variations in the water activity levels were attributable to the difference in packing configuration of the molecular structures. The MCC samples retained more bound water when compared with starch samples, possibly, because of a more tightly packed molecular array. However, moisture uptake effects were of minimal influence in this rheological study because the samples were successfully dried to values close to 4.0% (d.b.) and exhibited water activity values lower than 0.3 (Table 1). The mean volume diameters ($d_{4,3}$) of the samples differed significantly (Table 1, $p < .05$). All the starches' particle size distributions were bimodal while MCC sample was mono-disperse (Fig. 2a). Wider spans were observed for corn starch and MCC powders (Fig. 2b).

There were significant variations in the mean values of aspect ratio between dried starch powders and MCC powders due to differences in physicochemical properties and granule sources [13] (Table 1, $p <$ 005). As expected, MCC samples exhibited the highest shape irregularities followed by wheat starch (Fig. 2c, $p < .05$). No significant differences were found between corn and potato starches' mean aspect ratios (Table 1, $p > .05$). The micrographs in Fig. 3 supported the variability in aspect ratio. MCC presented rod-shape structures (Fig. 3a) while the starch particles were more rounded.

Table 1
Particle properties and moisture content values of the powder samples.

Sample	Moisture, before drying, 25 °C (d.b.,%)	Moisture, after drying, 25 °C (d.b., %)	Water activity, a_w [−], 25 °C	Volume mean diameter of dried samples ($d_{4,3}$, μm)	Mean aspect ratio of dried samples [−]
MCC PH101	4.56 ± 0.03^{d}	–	0.274 ± 0.005^{a}	93.14 ± 2.96^{a}	0.63 ± 0.005^{c}
Wheat starch	14.83 ± 0.13^{a}	4.65 ± 0.30^{a}	0.127 ± 0.003^{d}	34.60 ± 1.17^{c}	0.74 ± 0.009^{b}
Corn starch	10.02 ± 0.01^{c}	4.79 ± 0.12^{a}	0.239 ± 0.003^{b}	27.71 ± 1.72^{d}	0.77 ± 0.005^{a}
Potato starch	11.72 ± 0.28^{b}	4.66 ± 0.26^{a}	0.144 ± 0.001^{c}	50.30 ± 2.45^{b}	0.76 ± 0.012^{a}

Average values ± SD. Different lowercase letters in the same column indicate a statistically significant difference between samples.

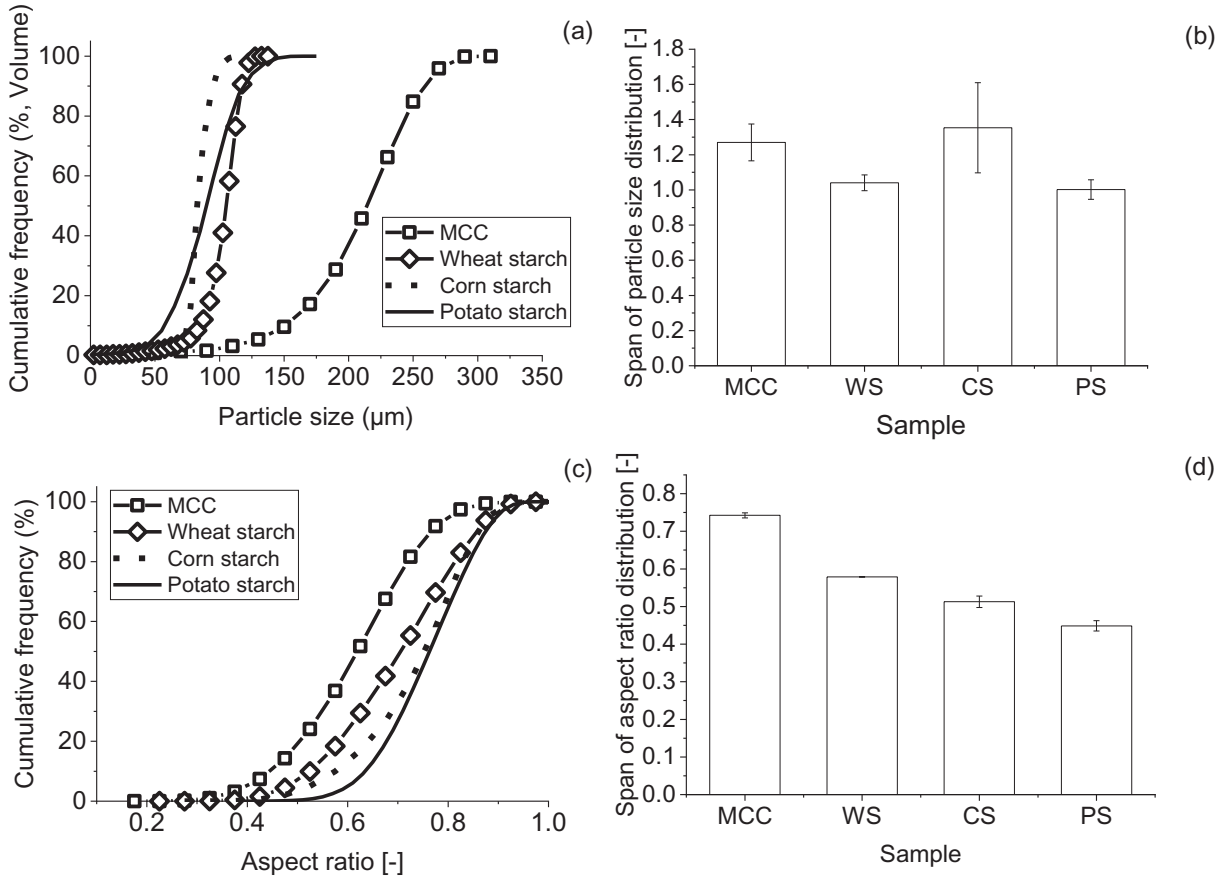

Fig. 2. Particle size and shape of the powder samples: (a) Particle size distribution of dried starches and MCC, (b) Span of particle size distributions for MCC PH101 and starch samples after drying to a moisture level of 4.64% (d.b.), (c) Particle shape distribution of dried starches and MCC, (d) Span of aspect ratio distribution for MCC PH101 and starch samples after drying to a moisture level of 4.64% (d.b.).

MCC is conventionally manufactured by treating alpha-cellulose microfibrils, constituting crystalline and amorphous domains, with an excess of mineral acids. The amorphous regions are hydrolyzed, yielding in cellulose microcrystallites that upon drying produce microcrystalline cellulose (powder grade) [14]. This inherent crystallinity helps explain the rod-shape of MCC granules.

The agglomerates found in wheat (>100 μm, Fig. 3b) and corn starch (>80 μm, Fig. 3c) particles are more branched as compared with potato starch (>100 μm, Fig. 3d) which had disc-like/lenticular arrangements. Baldwin et al. [15], using atomic force microscopy, observed rougher surfaces on potato starch granules than wheat starch. The roughness and shape characteristics, of both primary particles and agglomerates (in starch samples), are directly related to the particle properties, surface composition, degree of crystallinity, and their processing conditions during milling and drying [13]. The morphological variations can certainly influence the flow behavior and the shear input required to achieve robust processing conditions.

3.2. Compressibility profile

Potato starch sample exhibited relatively reduced compression profiles due to its larger particle size in comparison to the other starch systems (Fig. 4). The slight increase in the compressibility of wheat starch may be due to the rise of solid fraction comparatively to the corn starch powder bed. Bian et al. [16] also correlated an increase in solid fraction and distinct particle deformation profiles with the higher compressibility of soft white winter wheat flour against hard red winter wheat flour.

A significant difference in compressibility was observed between MCC and starch samples ($p < .05$). MCC sample's larger particle size and high aspect ratio justified its narrow compressibility range. In similar with the Warren Springs penetration stage (Section 3.3), the aspect ratio variations produced an interlocking effect as the normal load increased. This interlocking effect was prevalent over the entire range of stresses since the slope of the compressibility curve for MCC was lesser than for the starch powders. This implies that particle shape influences,

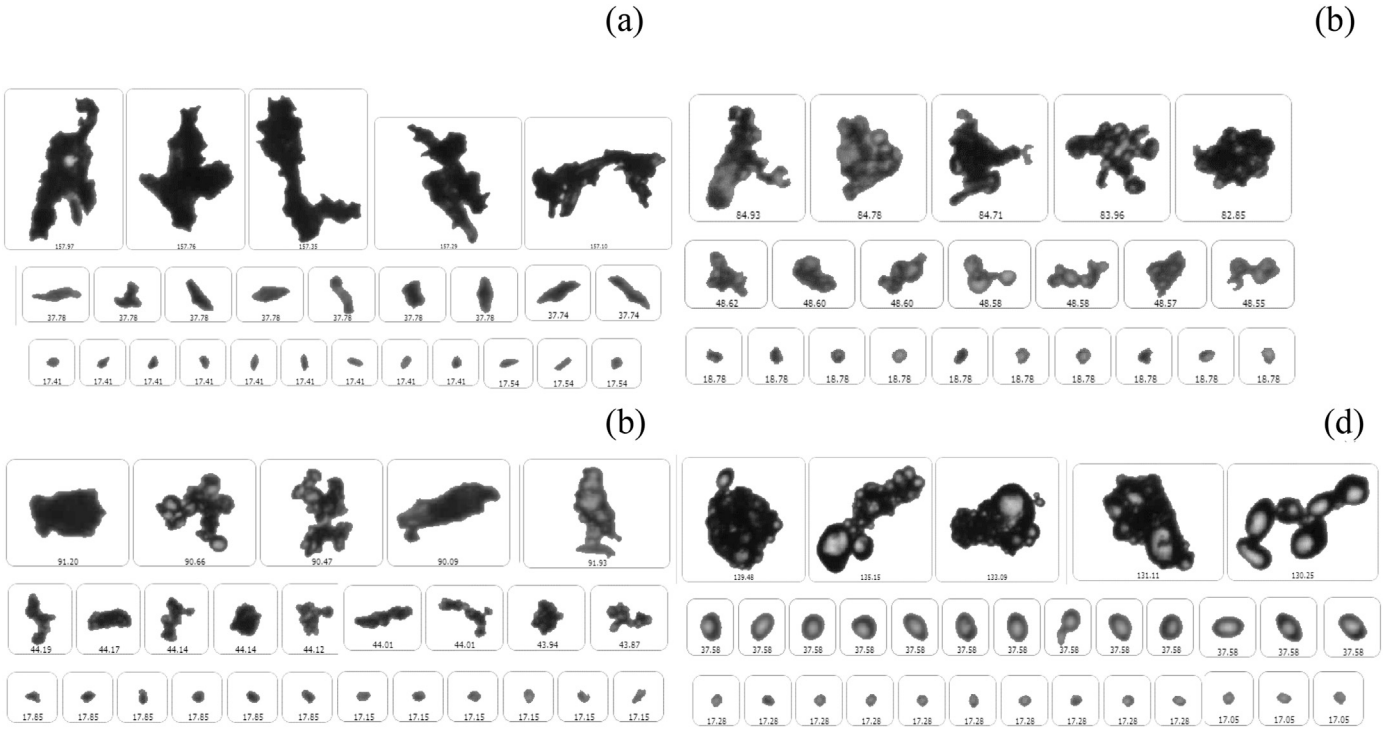

Fig. 3. 2-D images of the samples obtained via Morphologi-G3ID optical system set at × 5: (a) Microcrystalline cellulose (MCC), (b) Wheat starch , (c) Corn starch, (d) Potato starch. The subscript numbers refer to mean volume diameters ranging from 15 to 100 μm.

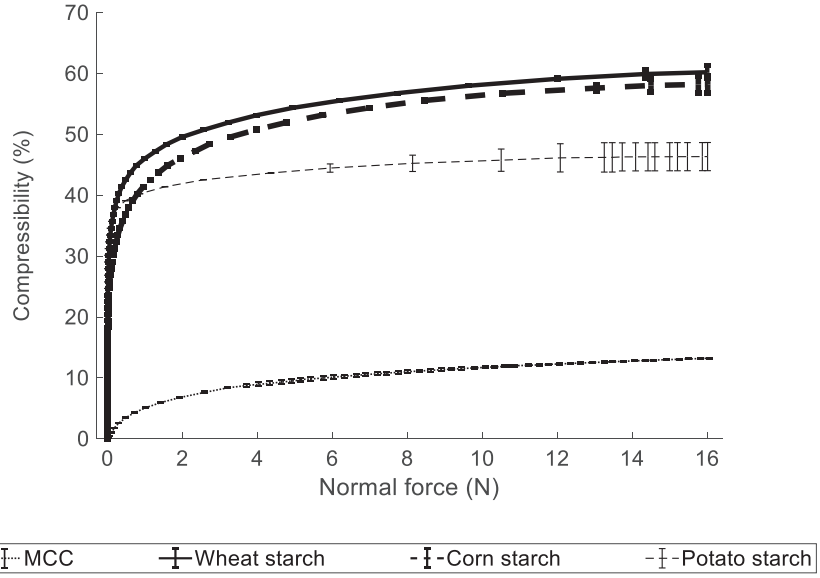

Fig. 4. Compressibility profile of powder samples.

in addition to the particle size, should be considered when optimizing powder flow under confined conditions.

3.3. Penetration profile

At both pre-compaction loads of 0.25 kPa and 3 kPa, a greater normal force was needed for the displacement of the Warren Springs geometry in MCC samples (Fig. 6). Mechanical interlocking of the rod-shaped structure justified the significant difference in the geometry's work displacement for the MCC powder relative to the starch powders (Fig. 5b, $p < .05$). The interlocking hindered a complete penetration of the geometry as detailed in Figs. 5 and 6a. In Fig. 6a, a slight increase in the penetration was observed from 0.25 to 0.5 kPa for the MCC sample followed by a subsequent decrease in penetration depth (1 and 3 kPa), which confirmed the rearrangement of sharp-edged particles and its effect on the poor flow performance. This phenomenon underestimated the cohesion strength values for MCC samples since the blade penetration was not complete (Fig. 6). Therefore, comparison between the cohesion strength of MCC and starch samples ought to be regarded with care.

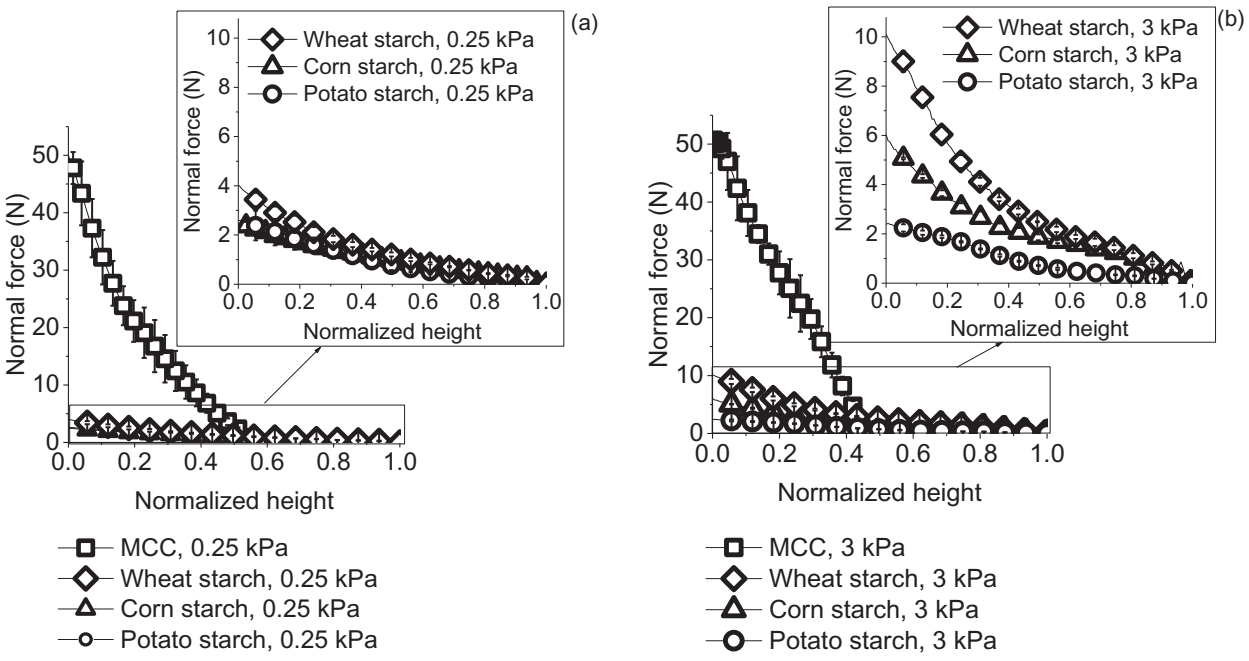

Fig. 5. Penetration profile of Warren Springs geometry for samples consolidated at a) 0.25 kPa and b) 3 kPa.

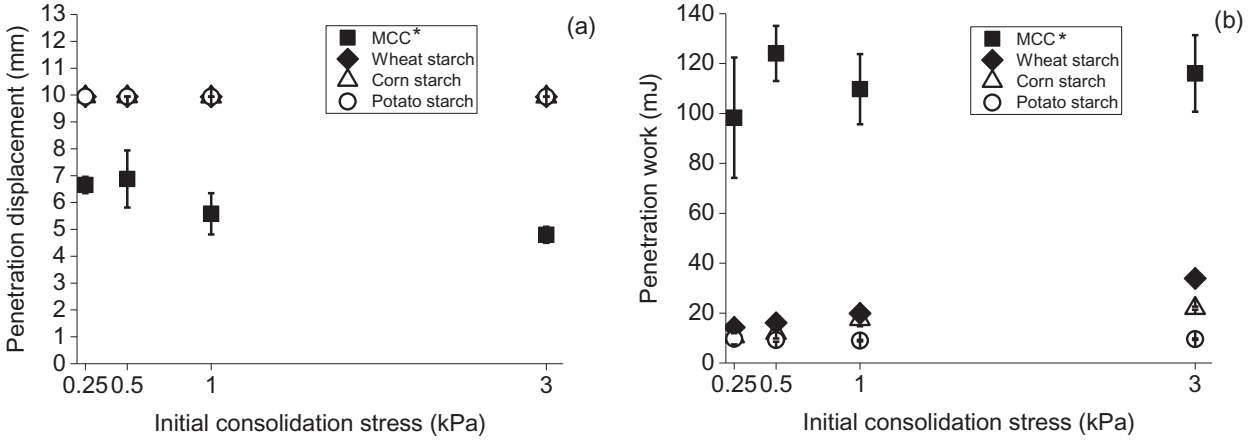

Fig. 6. Penetration profile of Warren Springs geometry: a) Penetration displacement at different pre-compaction loads, b) Penetration work derived from the area of normal force versus geometry displacement.

The penetration work on wheat and corn starches, obtained from the integration of the normal force versus height (mN.m or mJ), differed significantly from the potato starch sample in all pre-compaction stresses (Fig. 6b, $p < .05$). Evidently, in the case of starch powders, the large particle size of potato starch compared with other starch samples was a determinant factor to justify its lower penetration characteristics. Meanwhile, the high penetration work for wheat starch could be related to the significantly different mean aspect ratio values when compared with potato and corn starches (Table 1, $p > .05$). Furthermore, the penetration work correlated well with the cohesion trend (Fig. 7), which is indicative that the characteristic shape of wheat starch particles can contribute to an increase in interparticle interactions. Wheat and corn starches are known to have higher amylose content when compared with native potato starch [17]. Therefore, another reason for the characteristic penetration behavior could be different ratios of amylose and amylopectin, which may have resulted in distinct mechanical properties and, hence, different failure modes [18].

It is noteworthy that the penetration profile is responsible for pressure buildup and consequent increase in the normal stresses acting on the powder bed (Fig. 5). This signifies that the operational trend of the Warren Springs cohesion tester is characterized by sample over-consolidation as detailed in Section 2.4.

3.4. Effect of microstructure on the cohesion strength profile

The Warren Spring test is broadly described in literature to possess a similar momentum transfer as that of conventional ring shear cells, typically, operating at a normal load angularity of at least 45° [6]. This trend justified the consideration of radial force distribution along with the claim that the Warren Springs tester provides a qualitative description of cohesiveness in over-consolidated samples.

The cohesion strength profile of the samples at pre-compaction loads of 0.25 and 3 kPa are presented in Fig. 7. Regardless of the normal stresses applied during pre-compaction and penetration steps, the cohesion trend of starch samples was similar to that of MCC. However,

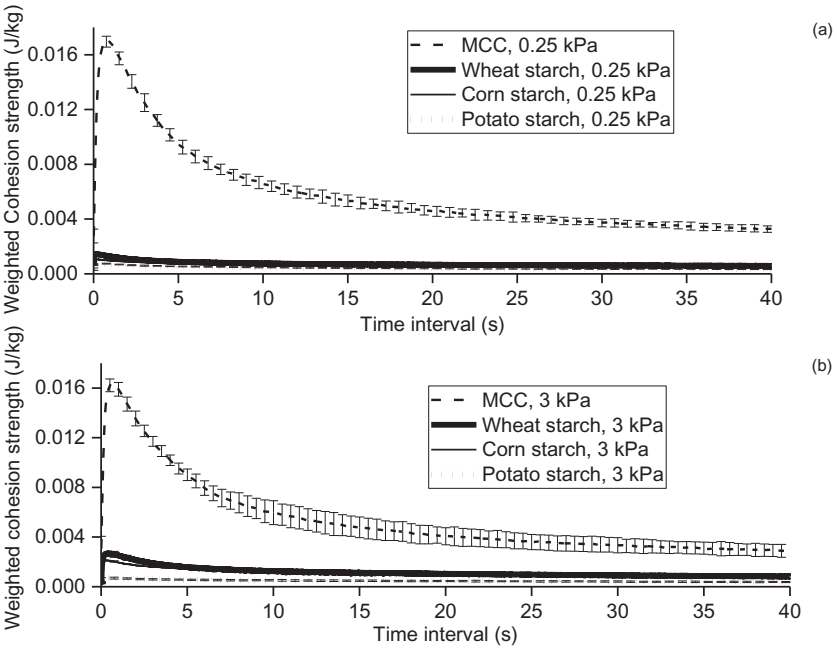

Fig. 7. Cohesion strength profile of samples at pre-compaction loads of a) 0.25 kPa and b) 3 kPa.

MCC samples exhibited the highest incipient peak followed by wheat, corn, and potato starches. The increased cohesion strength of over-consolidated MCC powder may not be due to the magnitude of intermolecular interactions, but instead due to the frictional instability from the brittle characteristics of the MCC particles [19].

The particle size, and the differences in shape characteristics justified the changes in cohesion strength profiles of the starch powders as denoted in Fig. 8. In this study, wheat starch showed a higher weighted peak cohesion when compared with corn and potato starches (Fig. 8). The smaller particle sizes and a higher specific surface area played an important role on the cohesiveness of wheat and corn starches that contributed to an additional interparticle interaction [20]. Furthermore, wheat starch is categorized in literature by short amylopectin branch chain length relative to corn starch, which presents an intermediate branch chain, and potato starch with the longest amylopectin branch chain [21]. Chiotelli & LeMeste [18] and Raeker et al. [22] have linked short and intermediate amylopectin branch chains and high amylose content with increasing crystallinity. The amylopectin component is responsible for the crystalline structure, while the amorphous amylose molecules are distributed across the amylopectin pockets. Differences in molecular structural arrangement may induce distinct physical and mechanical properties, which can explain the agglomeration trends as

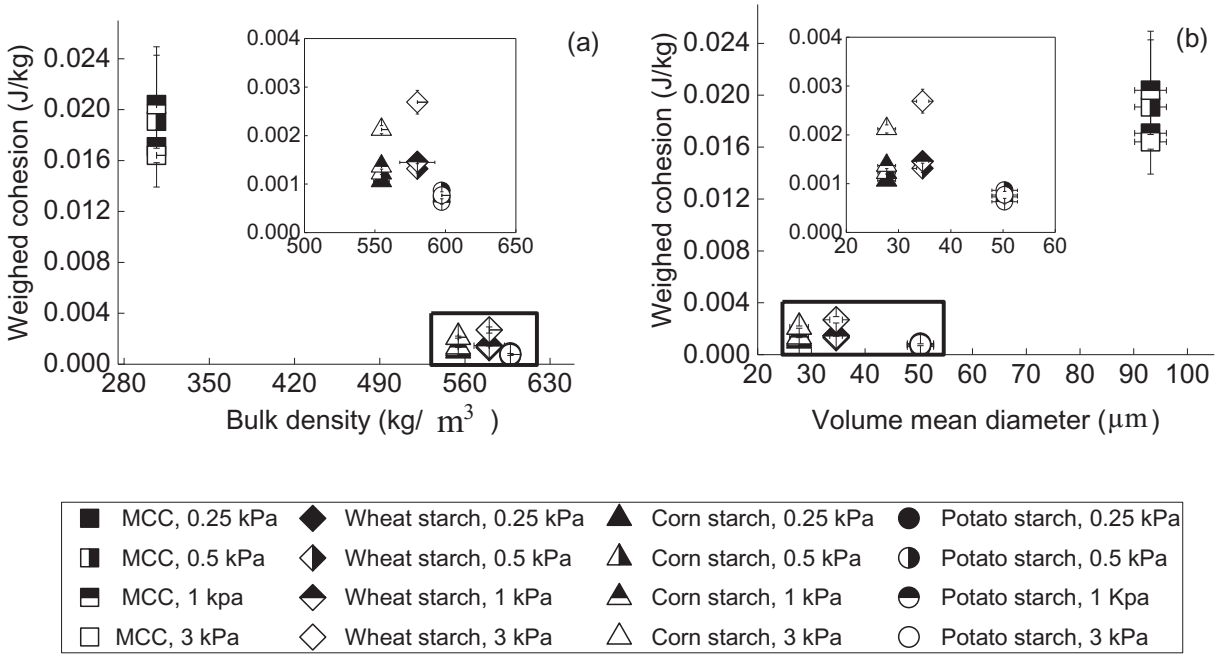

Fig. 8. Peak weighted cohesion values of samples as a function of a) bulk density and b) volume mean diameter.

well as the morphological variations in wheat, corn, and potato starches (Fig. 3). The dominance of crystallinity in wheat starch systems along with the high amylose content may have resulted in increased hardness and further resistance for probe displacement.

3.5. Effect of particle properties on the failure mechanism

Fig. 9 displays the difference between the incipient point and the minimum steady state point (at 40 s) during plastic deformation. Both values were derived from the weighted cohesion strength profile presented in Fig. 7. There was a significant difference between the incipient and plastic failure points of MCC and starch samples ($p < .05$). Eichhorn and Young [23] reported average Young's modulus values in the range of 25 ± 4 GPa for MCC. They also reported a direct proportionality between the Young's modulus of an MCC particle with its degree of crystallinity. Meanwhile, Schroeter et al. [24] presented Young's modulus value of 2.7 GPa for the potato starch particles (13% moisture content-d.b.). Stasiak et al. [25] indicated that the removal of water increases the elastic modulus of potato starch granules. However, the values were in a similar range of magnitude for those reported by Schroeter et al. [24]. Based on the micro-mechanics data described in the relevant literature, the peak cohesion of MCC sample was greater than that of the starch samples because of the stiffer particle surfaces and rod-shape particle configuration, which led to mechanical interlocking.

No visual differences from MCC, which exhibited a Hookean deformation profile [10], could be observed for the cohesion strength of starch powders. However, the transient failure mechanism (from incipient to steady flow mode) differed significantly between starch sources for all pre-compaction stresses ($p < .05$). The main reason for the difference in magnitude of incipient and steady state transition (Fig. 9) could be because of inherent agglomeration patterns (Fig. 3) of the different starch samples as well as due to their varied particle/agglomerate shapes and distinct post-compression solid fraction (Fig. 4). For example, the higher compression trends in wheat starch (Figs. 2c and 3b) potentially explains the higher gap required to achieve steady state stabilization, especially at increased normal loads (Fig. 9). Whereas, the rod-shape and larger particle sizes of MCC particles favoured a less compact powder bed that, consequently, contributed to a more prevalent and faster plastic transition when compared with the denser packing profiles for the starch samples as discussed in section 3.2 and Fig. 4. Fig. 9 suggests that after plastic failure, differences in particle morphological attributes and bed dilation dictated the kinetics towards flow stabilization. These results show the influence of particle size and shape distributions on the bulk level compaction as a result of distinct particle arrangement.

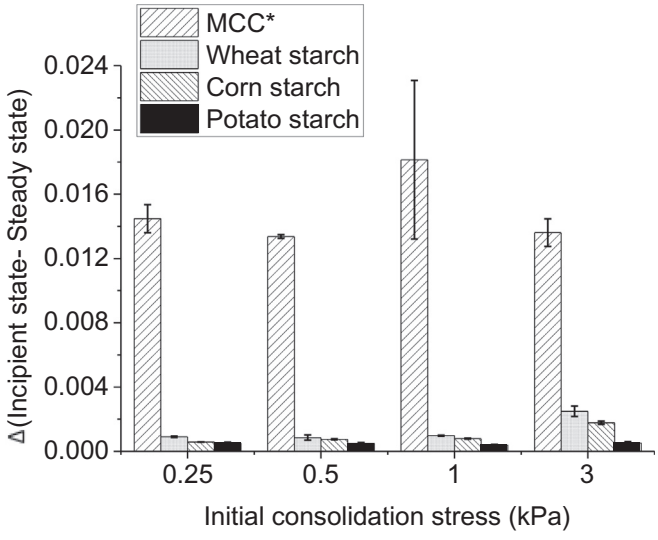

Fig. 9. Difference between incipient peak and minimum steady state point (at 40 s) derived from the weighted cohesion strength profile.

3.6. Predictive model

A statistical model that comprised of mean values of aspect ratio and particle size as the independent variables was developed to relate the weighted cohesion with particle properties (Eq. (5)):

$$S = \beta_0 + \beta_1 X_1 + \beta_2 X_2 + \beta_3 X_3 + \beta_4 X_4 + \epsilon \quad (5)$$

where, S is the value of the response variable, i.e., weighted cohesion (J/kg), X_1 is the aspect ratio [−], X_2 is the volume mean diameter ($d_{4,3}$, m), X_3 is the penetration work during the penetration step of the Warren Springs geometry (J), and X_4 is the span of the particle size distribution [-]. β_i are the parameters of the regression model (β_1 [J/kg], β_2[J/kg.m], β_3 [1/kg], β_4 [J/kg]), and ϵ is a random error term that follows a normal independent probability distribution with $E\{\varepsilon_i\} = 0$ and $\sigma^2\{\varepsilon_i\} = \sigma^2$ also expressed in units of J/kg.

Three transformations (logarithmic, square root, and weighted least squares) were tested for improving the predictability of the model. The best model parameters from the original model and the transformed models are presented in Table 2.

The predictive model and the model parameters do not include MCC data points. The exclusion of MCC was based on the limited penetration depth of the Warren Springs geometry as detailed in Section 3.3, which prevented an accurate comparison of the cohesion strength magnitudes between MCC and starch powders.

The penetration work as a predictive variable, derived from the penetration step of the Warren Springs' test, depended on factors such as internal friction coefficients, magnitude of interparticle interactions, and the mechanical strength of the powder bed. Whereas, the span of the size distribution was selected as an attempt to evaluate the effect of particle size distribution on the prediction of the cohesion strength. From a descriptive correlation analysis, the cohesion strength correlated better with the penetration work ($r = 0.94$) and the volume mean diameter ($r = -0.56$). Lower values of descriptive correlation were observed for averaged aspect ratio ($r = -0.35$) and size distribution span ($r = 0.16$). The best model, using the best subset selection, included the mean volume diameter (β_1) and the penetration work (β_3) as independent variables without transformation (model 1; Table 2). This model exhibited low extrinsic variability (MSE = $3.60^{*}10^{-8}$), relatively low C_p, which indicated reduced bias, and small PRESS values, which strengthened its predictive ability (Table 2). In addition, the model also presented considerably satisfactory coefficient of determination (R^2), capable of predicting 89.7% of the variability in cohesion strength of starch samples, and reduced multicollinearity likelihood (VIF = 1.24 i.e. VIF < 10).

The second- and third-best models, logarithmic and square root transformations of the independent variables, respectively, yielded in significance of the penetration work (β_3) (Table 2). However, the prediction of the variability in cohesion strength of these models decreased by 6% (model 2) and 11% (model 3) as compared with model 1. The remaining transformations exhibited a reduction in prediction of new observations as their prediction sum of square and mean square of error values increased (models 4, 5, 7–10).

A model optimization substituting the span of size by the span of the aspect ratio was also attempted. The selection of this new data set was based on the higher correlation between cohesion strength and the span of aspect ratio ($r = 0.66$). However, the best model remained the one with the inclusion of non-transformed independent variables mean volume diameter and penetration work. The C_p value was the only criterion that changed for the modified data set. The C_p value increased from 1.08 (data set that included span of size as an independent variable) to 1.90 (data set that included span of aspect ratio as an

Table 2
Statistical parameters used as cohesion prediction model via best subset selection criteria.

R^2	$R^2_{adjusted}$	C_P	PRESS	MSE	$\mathcal{B}_0$ (J/kg)	$\mathcal{B}_1$ (J/kg)	$\mathcal{B}_2$ (J/kg.m)	$\mathcal{B}_3$ (1/kg)	$\mathcal{B}_4$ (J/kg)
1- Non-transformed model: $S = \beta_0 + \beta_1 X_1 + \beta_2 X_2 + \beta_3 X_3 + \beta_4 X_4 + \epsilon$									
0.90	0.89	1.08	1.35E-06	3.60E-08	6.48E-04	−10.99	.	7.00E-02	.
2- Logarithmic transformation for independent variables: $S = \beta_0 + \beta_1 \log(X_1) + \beta_2 \log(X_2) + \beta_3 \log(X_3) + \beta_4 \log(X_4) + \epsilon$									
0.85	0.85	4E-03	1.98E-06	5.40E-08	6.92E-03	.	.	3.03E-03	.
3- Square root transformation for independent variables: $S = \beta_0 + \beta_1 \sqrt{(X_1)} + \beta_2 \sqrt{(X_2)} + \beta_3 \sqrt{(X_3)} + \beta_4 \sqrt{(X_4)} + \epsilon$									
0.81	0.80	1.287	2.74E-06	7.00E-08	3.86E-03	.	.	−3.12E-04	.
4- Logarithmic transformation for dependent variable: $\log(S) = \beta_0 + \beta_1 X_1 + \beta_2 X_2 + \beta_3 X_3 + \beta_4 X_4 + \epsilon$									
0.88	0.87	4E-03	0.16	4.38E-03	−2.246	−7816.3	−0.855	16.691	.
5- Logarithmic transformation for dependent and independent variables: $\log(S) = \beta_0 + \beta_1 \log(X_1) + \beta_2 \log(X_2) + \beta_3 \log(X_3) + \beta_4 \log(X_4) + \epsilon$									
0.86	0.85	2.11	0.18	5.08E-03	−3.388	−0.436	.	16.691	.
6- Weighing transformation for independent variables: $S = \beta_0 + \beta_1 W'_1(X_1) + \beta_2 W'_2(X_2) + \beta_3 W'_3(X_3) + \beta_4 W'_4(X_4) + \epsilon$									
0.53	0.48	3.318	6.46E-06	1.8E-07	9.459E-04	1.75E−11	.	3.22E-09	-1.65E-08
7- Square root transformation for independent variables: $\sqrt{S} = \beta_0 + \beta_1 X_1 + \beta_2 X_2 + \beta_3 X_3 + \beta_4 X_4 + \epsilon$									
0.86	0.84	3.03	224.21	6.02	−8.16	326,738.80	43.42	−455.26	.
8- Square root transformation for independent and dependent variables: $\sqrt{S} = \beta_0 + \beta_1 \sqrt{(X_1)} + \beta_2 \sqrt{(X_2)} + \beta_3 \sqrt{(X_3)} + \beta_4 \sqrt{(X_4)} + \epsilon$									
0.84	0.82	3.21	269.15	6.97	102.48	−0.120	−61.71	2.16	.
9- Weighing transformation for independent and dependent variables: $W'S = \beta_0 + \beta_1 W'_1(X_1) + \beta_2 W'_2(X_2) + \beta_3 W'_3(X_3) + \beta_4 W'_4(X_4) + \epsilon$									
0.30	0.25	1.11	1.16E + 16	3.03E + 14	26,396,906.64	−1.23	.	.	−697.37
10- Weighing transformation for dependent variable: $W'S = \beta_0 + \beta_1 X_1 + \beta_2 X_2 + \beta_3 X_3 + \beta_4 X_4 + \epsilon$									
0.26	0.22	1.12	1.23E + 16	3.16E + 14	66,515,268.42	−1.08E + 12	.	1,265,805,935.00	.

$\mathcal{B}_1$ is associated with d_{34}, $\mathcal{B}_2$ is associated with the aspect ratio, $\mathcal{B}_3$ is associated with the penetration work of the Warren Springs geometry, and $\mathcal{B}_4$ with the span of the particle size distribution.

independent variable). Despite the influence of aspect ratio on powder flowability as detailed in relevant literature [4,26], neither the mean values of aspect ratio nor the span of the shape factor was included in this predictive model. This is because the penetration work already accounted for the frictional variations due to the morphological effects.

4. Conclusions

This study provided relevant information on the cohesiveness of starch powders and MCC PH101 based on their physical characteristics that could be important in distinguishing the use of these powders as fillers and bulk agents. MCC PH101 exhibited high Warren Spring penetration work, high weighted cohesion peaks, and low compressibility profiles. The mechanical interlocking from the rod-shaped particles may have had a predominant effect on the rheological profile of MCC PH101. Meanwhile, among the starch samples, wheat starch had the highest values of penetration work and peak cohesion followed by corn and potato starches. Wheat starch was also more compressible. The molecular makeup of starch granules may have contributed to the shape characteristics, mechanical properties, and the inherited agglomeration trend. The differences in particle characteristics justified the distinct flow modes observed for starch samples when compared with the MCC powder sample.

A statistical model accounting for the penetration work and volume mean diameter effects was developed to predict the cohesiveness of starch powders. The advantage of this model includes that it considers the effects of the magnitude of interparticle interactions and the change in mechanical strength of the powder bed with the downward motion of the Warren Springs geometry during penetration step.

Overall, this study helped understand the impact of solid-state matrix on the kinematic profiles of different powder samples at high strain conditions. The differences in failure mode can be further explored for a direct quantification of the effect of micro-mechanical and shape properties of powders on their bulk properties, such as cohesion and compressibility. This powder characterization methodwill be valuable to understand powder flow in unit operations such as high shear granulation, mixing, and compaction. However, this methodology cannot be adapted for hopper and silo designs which rely on low strain measurements such as those used in shear cells.

Declaration of Competing Interest

The authors declare that they have no known competing financial interests or personal relationships that could have appeared to influence the work reported in this paper.

References

[1] K. Siliveru, C.G. Jange, J.W. Kwek, R.P.K. Ambrose, Granular bond number model to predict the flow of fine flour powders using particle properties, J. Food Eng. 208 (2017) 11–18.
[2] C.G. Jange, R.P.K. Ambrose, Effect of surface compositional difference on powder flow properties, Powder Technol. 344 (2019) 363–372.
[3] D.V. Neel, R.C. Hoseney, Sieving characteristics of soft and hard wheat flours, Cereal Chem. 61 (1984) 259–261.
[4] F. Podczeck, Y. Miah, The influence of particle size and shape on the angle of internal friction and the flow factor of unlubricated and lubricated powders, Int. J. Pharm. 144 (1996) 187–194.
[5] C. Jacquot, J. Petit, F. Michaux, E.C. Montes, J. Dupas, V. Girard, A. Gianfrancesco, J. Scher, C. Gaiani, Cocoa powder surface composition during aging: a focus on fat, Powder Technol. 292 (2016) 195–202.
[6] D. Schulze, Powders and Bulk Solids: Behavior, Characterization, Storage and Flow, Springer Science & Business Media, New York, NY, 2008.
[7] K. Pardikar, C. Wassgren, Predicting the critical outlet width of a hopper using a continuum finite element method model, Powder Technol. 356 (2019) 649–660.
[8] M. Peleg, M.D. Normand, M.G. Corradini, Interactive software for calculating the principal stresses of compacted cohesive powders with the Warren-spring equation, Powder Technol. 197 (2010) 268–273.
[9] D. Geldart, E.C. Abdullah, A. Verlinden, Characterisation of dry powders, Powder Technol. 190 (2009) 70–74.
[10] J.L.R. Orband, D. Geldart, Direct measurement of powder cohesion using a torsional device, Powder Technol. 92 (1997) 25–33.
[11] ISO, ISO 13322-2 standard test method for image particle size analysis, ISO Standards, International Organization for Standardization, Geneva, Switzerland 2006, p. 2006.
[12] I. Mishra, P. Liu, A. Shetty, C.M. Hrenya, On the use of a powder rheometer to probe defluidization of cohesive particles, Chem. Eng. Sci. 214 (2020) 11522.
[13] M. Schirmer, A. Höchstötter, M. Jekle, E. Arendt, T. Becker, Physicochemical and morphological characterization of different starches with variable amylose/amylopectin ratio, Food Hydrocoll. 32 (2013) 52–63.
[14] G. Thoorens, F. Krier, B. Leclercq, B. Carlin, B. Evrard, Microcrystalline cellulose, a direct compression binder in a quality by design environment- a review, Int. J. Pharm. 473 (2014) 64–72.
[15] P.M. Baldwin, J. Adler, M.C. Davies, C.D. Melia, High resolution imaging of starch granule surfaces by atomic force microscopy, J. Cereal Sci. 1998 (27) (1998) 255–265.
[16] Q. Bian, S. Sittipod, A. Garg, R.P.K. Ambrose, Bulk flow properties of hard and soft wheat flours, J. Cereal Sci. 63 (2015) 88–94.
[17] P.V.F. Lemos, Characterization of amylose and amylopectin fractions separated from potato, banana, corn, and cassava starches, Int. J. Biol. Macromol. 132 (2019) 32–42.

[18] E. Chiotelli, M. LeMeste, Effect of small and large wheat starch granules on thermo-mechanical behavior of starch, Cereal Chem. 79 (2002) 286–293.
[19] G. Thoorens, F. Krier, E. Rozet, B. Carlin, B. Evrard, Understanding the impact of microcrystalline cellulose physicochemical properties on tabletability, Int. J. Pharm. 490 (2015) 47–54.
[20] V. Landillon, D. Cassan, M. Morel, B. Cuq, Flowability, cohesive, and granulation properties of wheat powders, J. Food Eng. 86 (2008) 178–193.
[21] Y. Liu, K. W. Perry. Ng., Isolation and characterization of wheat bran starch and endosperm starch of selected soft wheats grown in Michigan and comparison of their physicochemical properties, Food Chem. 176 (2015) 137–144.
[22] M.O. Raeker, C.S. Gaines, P.L. Finney, T. Donelson, Granule size distribution and chemical composition of starches from 12 soft wheat cultivars, Cereal Chem. 75 (1998) 721–728.
[23] S.J. Eichhorn, R.J. Young, The Young's modulus of a microcrystalline cellulose, Cellulose 8 (2001) 197–207.
[24] J. Schroeter, M. Hobelsberger, B. Reichenhall, On the mechanical properties of native starch granules, Starch 44 (1992) 247–252.
[25] M. Stasiak, M. Molenda, J. Horabik, P. Mueller, I. Opalinski, Mechanical properties of potato starch modified by moisture and addition of lubricant, Int. Agrophys. 28 (2014) 501–509.
[26] T. Horio, M. Yasuda, S. Matsuka, Effect of particle shape on powder flowability of microcrystalline cellulose as determined using the vibrational shear tube method, Int. J. Pharm. 473 (2014) 572–578.